RESEARCH ARTICLE

Phonons investigation of ZnO@ZnS core-shell nanostructures with active layer

Branka Hadzic[1] | Branko Matovic[2] | Marjan Randjelovic[3] |
Radmila Kostic[1] | Maja Romcevic[1] | Jelena Trajic[1] | Novica Paunovic[1] |
Nebojsa Romcevic[1]

[1]Institute of Physics, University of Belgrade, Belgrade, Serbia

[2]Institute Vinca, University of Belgrade, Belgrade, Serbia

[3]Faculty of Sciences and Mathematics, University of Nis, Nis, Serbia

Correspondence
Maja Romcevic, Institute of Physics, University of Belgrade, 11080 Belgrade, Serbia.
Email: romcevic@ipb.ac.rs

Abstract

In the present work experimental study of the ZnO@ZnS core-shell nanostructure with an active layer obtained by conversion of zinc oxide powders with H_2S is reported. The prepared structures were characterized by scanning electron microscopy, X-ray diffraction, Raman spectroscopy, and far-infrared spectroscopy. Top surface optical phonon (TSO) in ZnO, characteristic for the cylindrical nano-objects, the surface optical phonon (SOP) mode of ZnS, and SOP modes in ZnO@ZnS core-shell nanostructure are registered. Local mode of oxygen in ZnS and gap mode of sulfur in ZnO are also registered. This result is due to the existence of an active layer in the space between ZnO core and ZnS shell, which is very important for the application of these materials as thermoelectrics.

KEYWORDS
active layer, core-shell nanostructures, local mode, surface phonons, thermoelectric

1 | INTRODUCTION

ZnO and ZnS are two well-known and widely used wide-band gap semiconductors that are still in the focus of scientific research. Different combinations and changeable structures of ZnO and ZnS intrigue researchers all over the world due to the large possibility of their application as optoelectronic devices, sensors, lasers, and other novel devices. Both materials, ZnO and ZnS, are abundant, highly stable, non-toxic, environmentally friendly and intensively studied II-VI materials.[1-3] They can exist in the form of three crystallographic phases: cubic sphalerite, hexagonal wurtzite, or, in the rarest form, cubic rock salt. ZnO at the room temperature preferentially crystallizes in the hexagonal phase, while the ZnS structure depends on the temperature. At the room temperature ZnS crystallizes in the cubic phase but at temperatures above 1020°C ZnS is most stable in the hexagonal phase

form. However, there are also other differences between these two materials besides the difference in existing phases at room temperature. Although both of these materials are characterized by the wide direct band gaps, ZnS shows wider direct band gaps for both of its crystallographic phases. Nevertheless, ZnO is characterized by higher exciton binding energy. Band gaps for the ZnO hexagonal phase are reported to be 3.34, 3.37, and 3.4 eV with the binding energy of 60 mW, for the ZnS cubic phase band gaps are 3.54 and 3.68 eV, while for the ZnS hexagonal phase are 3.80 and 3.91 eV with the binding energy of 40 mW.[4-8]

Excellent features of ZnO and ZnS as individual components contribute to the favorable properties of the materials obtained combining these two components and make them good candidates for a wide range of applications, such are the thermoelectric components.[9,10] The most important parameter in the field of

thermoelectricity is the so-called figure of merit. It provides a connection between the material parameters and the maximum efficiency that will be achieved when this material is used as a thermoelectric generator. The goal of designing new materials or structures is to keep the phonon part of thermal conductivity in the material as small as possible, without changing the electrical parameters (electric conductivity, Seebeck coefficient, and electronic part of thermal conductivity). One possible way to achieve this is to use a ZnO/ZnS superlattice.[11] Another possibility is to use $ZnO_{1-x}S_x$ alloys. In the latter case, impurities act as local scatters that can alter the phonon transport.[12]

The general conclusion of all of the previously mentioned studies is summarized in the work of Bachmann et al.[13] where it is underlined that incorporation of sulfur in ZnO and incorporation of oxygen in ZnS can substantially reduce the thermal lattice conductivity and increase the figure of merit. However, a possible breakthrough in this field can be achieved with the usage of ZnO@ZnS core-shell system.

Core-shell nanostructures are a special class of the biphasic materials whose properties depend not only on the combination of the core and shell materials but also on their geometry, design, and core-shell volume ratio.[14–18] In previous studies of the ZnO@ZnS core-shell structures, this phenomenon was disregarded.[19–24] So far, the research focus was on the methods of synthesis and the quality of the spatial homogeneity of the obtained structures, such are the attempts to eliminate the existence of impurity throughout the system.

In addition, the focus has been on the application of these structures in solar cells,[23] as new materials for luminescence, and for magnetic applications.[24] Characterization methods were also selected for this purpose. Spectroscopic methods were used only to confirm X-ray measurements. Thus, in Sundararajan et al.[19] it was said that the Fourier-transform infrared spectroscopy (FT-IR) spectra confirmed starching vibrations of ZnO and ZnS, respectively. In Flores et al.[20] the same conclusion was reached using Raman spectroscopy. No attention was paid to the possibility of the formation of any layer between the ZnO core and the ZnS shell, which is the topic of our research.

While scanning electron microscopy, X-ray diffraction (XRD) and far-infrared spectroscopy give us information about the global structure, Raman spectroscopy is focused on the local environment, which is crucial for this type of research. The present work aims to determine the existence of the active layer doping phases in the space between the core and the shell by registering the surface, local, and gap modes, as well as by analyzing other structural and optical characteristics of the ZnO@ZnS core-shell system.

2 | EXPERIMENT

For the synthesis of ZnO/ZnS core-shell nanostructures, gas-phase sulfidation of ZnO (Merck) at elevated temperatures was exploited using flow reactor which is schematically presented in Figure S1 (Supporting Information). Hydrogen sulfide was initially obtained from iron (II) sulfide and hydrochloric acid and without further processing was introduced in the round-bottom flask containing 3 g of ZnO powder. Iron sulfide was added into a three neck round bottom flask (B) with mounted dropping funnel with Polytetrafluoroethylene (PTFE) key (A) containing 3 M HCl. Flow of HCl was adjusted to achieve required H_2S flow of 6.5 ml/min during 6 h. Evolved gas was passed into round-bottom flask with ZnS (C) which was heated at 340–400°C. Vinyl laboratory tubings were used to introduce gas into flow reactor.

Unreacted H_2S was collected and retained in two stages. First, the vessel containing $FeCl_3$ solution (D) was used to chemically convert H_2S gas into iron sulfides and small amount of remaining gas was caught in the next stage using solution of NaOH (E).

Morphology of the obtained powders and their evolution during calcination were studied by the field emission scanning electron microscope (FE-SEM) model FE-SEM JEOL-5200F (Japan).

The composition of investigated samples was investigated utilizing a Rigaku IV XRD diffractometer with Cu Kα radiation at room temperature. The present phases were identified by applying the PDXL2 software (version 2.0.3.0),[25] with the reference to the diffraction patterns present in the International Centre for Diffraction Data (ICDD).[26]

The far-infrared reflection spectra were measured at room temperature at the spectral range from 70 to 630 cm^{-1} with a BOMEM DA 8 spectrometer.

The micro-Raman spectra were taken in the backscattering configuration and analyzed by the TriVista 557 system equipped with a nitrogen-cooled charge-coupled-device detector. As an excitation source the Verdi G optically pumped semiconductor laser with the 532 nm line was used. Excitation energy is in the off-resonance regime for all the considered materials.

3 | RESULTS

SEM images of the two starting materials (ZnO and ZnS nanoparticles) and the obtained core-shell structure

(ZnO@ZnS) are given in Figure 1. In Figure 1a large ZnO particles are shown, in Figure 1b long narrow ZnS particles can be observed, while in Figure 1c large particles of the formed core-shell ZnO@ZnS structure are evident. This is confirmation that the core-shell structure usually shows the same morphology as a core. ZnO particles are cylindrical with the diameter ranging from 200 to 500 nm and length in the 300 to 500 nm range. ZnS particles are spiral wire-shaped structures with the diameter in the 20 to 30 nm range and length in the 300 to 500 nm range. The final structure contains mostly ZnO cylinders that originate from the starting ZnO material. ZnS is probably located at the surface of ZnO cylinders as a shell.

The formation of ZnS layer around ZnO particle surface is well known from sulfidation reaction: $ZnO(s) + H_2S(g) = ZnS(s) + H_2O(g)$, where ZnS growth an outward development during ZnO sulfidation. Such a process leads to a core-shell structure, which has been clearly demonstrated in many studies.[27–29]

The X-ray diffractograms of ZnO, ZnS nanoparticles, and ZnO@ZnS core-shell nanostructure are shown in Figure 2. The detailed phase composition investigations revealed the presence of crystalline phases of the hexagonal ZnO and cubic ZnS compounds in the starting materials, while in ZnO@ZnS the cubic ZnS transformed into hexagonal polymorph. Cubic-to-hexagonal phase transition of ZnS has been observed at very low temperatures at 250°C.[30] Since the experiment is conducted in range of 340–400°C, it is normal that a phase transformation takes place.

The plane identification (indexing) is done. The diffraction peaks correspond to the (1 1 1), (2 2 0), and (3 1 1) planes of the cubic phase of ZnS, matching with JCPDS 05-0566, and wurtzite (hexagonal phase) was found in JCPDS 36-1450. The XRD peaks are broadened because of nanocrystalline nature of the synthesized samples. On the other side, ZnO phase is hexagonal wurtzite phase, (JCPDS 01-089-0510). Obtained the core-shell structure consists of 88% ZnO (in core) and 12% ZnS

(shell). Williamson-Hall plots were used to separate the effect of the size and strain in the nanocrystals.[31] The results are shown in Table 1.

By means of the PDXL2 software (version 2.0.3.0),[25] it was calculated that the mean crystalline size $\tilde{a}$ of ZnO is determined as 57 nm, in the case of ZnS is 2.1 nm, while obtained the core-shell structure consists of 88% ZnO (core) with mean crystalline size of about 67 nm
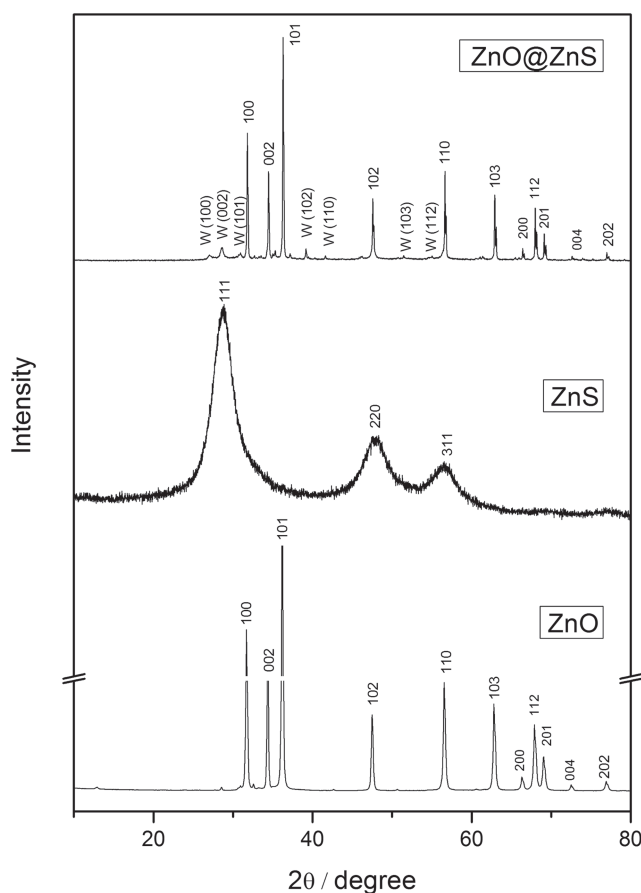
FIGURE 2 XRD spectra for all investigated samples. W = wurtzite (hexagonal) ZnS
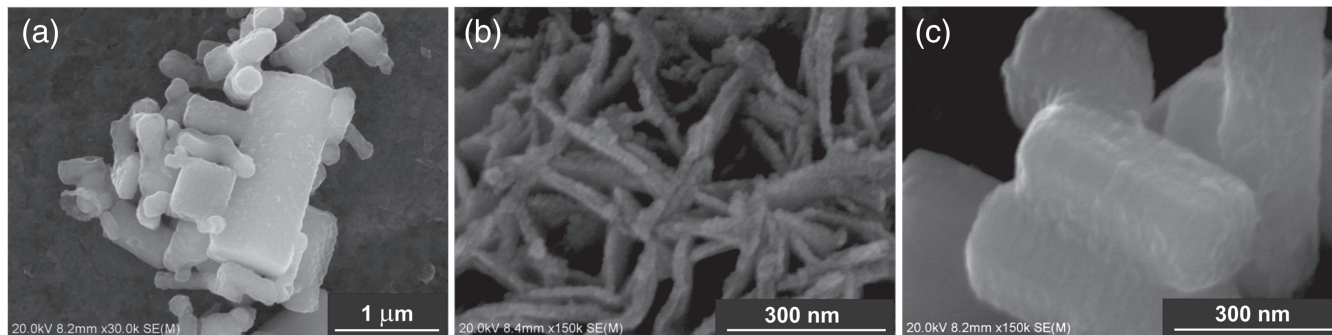
FIGURE 1 SEM images for (a) ZnO, (b) ZnS, and (c) ZnO@ZnS

TABLE 1 Unit cell parameters, crystallite size, and lattice strain of samples

Sample	Lattice parameter (nm)	Crystallite size (nm)	Strain (%)
starting material			
ZnS	$a = 0.53805(3)$	2.1	0.0075
ZnO	$a = b = 0.32521(4)$ $c = 0.52101$ (8)	57	0.145
ZnO@ZnS core-shell			
ZnS	$a = b = 0.3848$ $c = 0.6317$ $\alpha = 90$ $\beta = 90$ $\gamma = 120$	11	0.001884
ZnO	$a = b = 0.32481(4)$ $c = 0.520044(7)$	69	0.00072

and 12% ZnS (shell) with mean crystalline size of about 11 nm.

The lattice strain of phases in core-shell structure is 0.001884 for ZnS and 0.00072 for ZnO. The value for stress in case of ZnS phase is lower than the stress for ZnO. It can be considered to be the consequence of an ordering of atomic arrangement during sulfidation, that is, the formation of zinc sulfide. The less ordering lead to an increasing strain due to the significant amount of strain that is localized at the surface of crystallites as a result of a high concentration of broken bonds.

The hexagonal phase of ZnO, the cubic, and hexagonal phase of ZnS were previously registered by the XRD analysis. Since the understanding of the bulk material vibrational properties is crucial for the analysis of the vibration properties of the core-shell structure, the vibrational properties analysis was initiated with a brief report of the literature data for the registered phases. The bulk modes are expected to be shifted and broadened as a consequence of the miniaturization.

The hexagonal structure of ZnO belongs to the space group C_{6v}^4, with the unit cell that contains four atoms, where all atoms occupy C_{3v} sites. From the factor group theory analysis existence of nine optical modes, that are classified by the following symmetries $\Gamma_{opt} = A_1 + 2B_1 + E_1 + 2E_2$, is evident.[32] Modes of symmetry A_1, E_1, and E_2 are Raman active, A_1 and E_1 are infrared active, while B_1 is inactive (silent) mode. Both A_1 and E_1 are polar modes and split into transverse (TO) and longitudinal (LO) phonons with different wavenumbers due to the macroscopic crystal field. Anisotropy of the ZnO crystal causes A_1 and E_1 modes to have different wavenumbers.

The cubic ZnS structure belongs to $F-43m$ (T_d^2) space group with a trigonal primitive unit cell containing one formula unit with two atoms. Thus, it has 6 degrees of freedom, three acoustic, and three optical phonons. The Brillouin zone center phonons, both acoustic and optical, are triply degenerate for this cubic structure and

have symmetry species $\Gamma_{15}(F_2)$. A macroscopic electric field in polar crystals, such as ZnS, is associated with LO vibrations and makes LO mode energy greater than the TO mode energy. This effect removes the degeneracy of the optical mode yielding a doubly degenerate TO mode and a LO mode. Both, the TO and LO modes are Raman active, while the TO mode is also infrared active.[33,34]

Wurtzite ZnS belongs to the space group P63mc (C46r) and all atoms occupy C3r sites. The nine possible optic modes of the four-atom primitive cell have the following symmetries: $1A_1 + 2B_1 + 1E_1 + 2E_2$. The A_1 and E_1 branches are both Raman and IR active, the E_2's are only Raman active, and the B_1's are neither IR nor Raman active.

3.1 | Far-infrared spectroscopy

The experimental data of two starting materials and the obtained core-shell structure are presented by circles in Figure 3. To analyze the far-infrared spectra the standard analysis, which applies the correlation between the reflection coefficient and dielectric function, was used. A theoretical model of the bulk dielectric function was discussed by several authors.[35,36]

The low-frequency dielectric properties of the single crystals are described by classical oscillators corresponding to the TO-modes, to which the Drude part is superimposed to take into the account the free carrier contribution:

$$\varepsilon_S(\omega) = \varepsilon_\infty + \sum_{k=1}^{l} \frac{\varepsilon_\infty S_k}{\omega_{TOk}^2 - \omega^2 - i\gamma_{TOk}\omega} - \frac{\varepsilon_\infty \omega_P^2}{\omega(\omega + i\Gamma_P)} \quad (1)$$

where ε_∞ is the bound charge contribution and it is assumed to be a constant, $\omega_{TOk}\omega_{TOk}$ is the transverse optical-phonon wavenumber, $\omega_P\omega_P$ the plasma
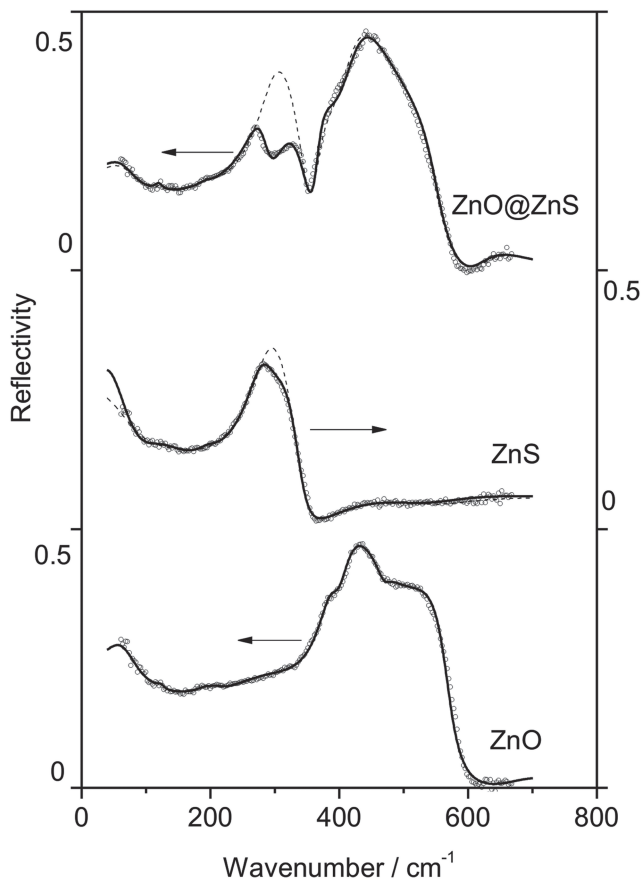
FIGURE 3 Far-infrared reflection spectra for all investigated samples. The experimentally obtained data points are depicted by circles. The theoretical spectra given as the solid lines are obtained with the model defined by Equations (1) and (2) and the fitting procedure

wavenumber, γ_{TOk} is damping, Γ_P is the plasmon mode damping coefficient, and S_k is an oscillator strength.

In general, the optical properties of an inhomogeneous material are described by the complex dielectric function that depends on the 3-D distribution of constituents. The investigated mixture consists of two dielectric components. One is treated as a host, and the other as the inclusion. The characterization of the inhomogeneous material by the two dielectric functions is not useful since the exact geometrical arrangement of the constituents of the material is needed. However, if the wavelength of the electromagnetic radiation is much larger than the size of inclusions, classical theories of inhomogeneous material presume that the material can be treated as a homogeneous substance with an effective dielectric function. In the literature, many mixing models can be found for the effective permittivity of such a mixture.[37] The optical properties of such materials depend

upon the properties of constituents, as well as their volume fraction.

The simplest model that describes an inhomogeneous material by an effective dielectric function can be written as $\varepsilon_{eff} = (1 - f) \, \varepsilon_1 + f \, \varepsilon_2$. This model is applicable in the case of bulk materials of dielectric constant ε_1 in which the second phase or the material of the dielectric constant ε_2, which occupies volume fractions f, is randomly distributed. In the case where nanoparticles are distributed in the air, or in an optically similar medium, the Maxwell–Garnett or Bruggeman formula is usually used.[37]

In general terms, the Maxwell–Garnett Effective Medium Approximation is expected to be valid at relatively low volume fractions f, since it is assumed that the domains are spatially separated and electrostatic interaction between the chosen inclusions and all other neighboring inclusions is neglected.

Since samples used in the present study are well defined with separated nanosized grains (as demonstrated on SEM images presented in Figure 1), the Maxwell–Garnet model was used for the present case. Effective permittivity of mixture, ε_{eff}, according to the Maxwell–Garnet mixing rule is as follows[38]:

$$\varepsilon_{eff} = \varepsilon_1 + 3f\varepsilon_1 \frac{\varepsilon_2 - \varepsilon_1}{\varepsilon_2 + 2\varepsilon_1 - f(\varepsilon_1 - \varepsilon_2)} \qquad (2)$$

In this case, nanoparticles of permittivity ε_2 are located randomly in the homogeneous environment ε_1 (air) and occupy a volume fraction f.

Solid lines presented in Figure 3 are calculated spectra obtained by a fitting procedure based on the previously presented model. The parameter adjustment was carried out automatically, using the least squares fitting of the theoretical (R_t) and experimental (R_e) reflectivity at q arbitrarily taken points:

$$\delta = \sqrt{\frac{1}{q} \sum_{j=1}^{q} \left(R_{ej} - R_{tj} \right)^2} \qquad (3)$$

The value of δ was minimized until it complied with the commonly accepted experimental error (less than 3%). For all the samples the determination errors of wavenumber and damping coefficients were in the range 3%–6% and 10%–15%, respectively. The agreement of the theoretical model obtained in this manner with the experimental results is excellent. In Table 2, the best fitting parameters are presented. In this case, the wavenumber indicated by ω_{TOk} in Equation 1 is perceived as the characteristic wavenumber for a given material.

TABLE 2 Calculated fit parameters obtained from the Raman and far-infrared spectra

	ZnS		ZnO		ZnO@ZnS		Description
	Raman (cm^{-1})	IR (cm^{-1})	Raman (cm^{-1})	IR (cm^{-1})	Raman (cm^{-1})	IR (cm^{-1})	
ω_P	-	82	-	94	-	91	
ω_1	132	119					[TO$_1$–LA]$_\Sigma$ or 2TA$_2$
ω_2	145				152		[TO$_u$–LA]$_\Sigma$
ω_3	157						[LO–LA]$_\Sigma$
ω_4	174						2TAX
ω_5			203	210	203	190	2TA or E$_2$(low)
ω_6	206	197			219		LA
ω_7					**246**		**Gap-mode S in ZnO**
ω_8	263	281				269	TO
ω_9	**310**	**309**			**305**	**301**	**SOP**
ω_{10}			330	338	334		E$_2$(high)–E$_2$(low)
ω_{11}	**346**	**350**			**349**	**357**	**LO and LO+Plasma (IR)**
ω_{12}			379	379	380	386	A$_1$(TO)
ω_{13}			411	395	409	410	E$_1$(TO)
ω_{14}	415	420					(LO$_\Gamma$ + TA$_L$) or (TO$_\Gamma$ + LA$_L$)
ω_{15}			436	436	436	438	E$_2$(high)
ω_{16}					**472**		**Local-mode O in ZnS**
ω_{17}			**484**	**469**			**TSO**
ω_{18}			**540**		**537**		**SOP**
ω_{19}			578	557	584	557	A$_1$(LO)

The parameters important for discussion are bold.

In Figure 3, the some phonon influence is evident at approximately 310 cm^{-1}. The experimental spectra are in complete agreement with the theoretical ones (please notice the solid lines in Figure 3) when the existence of this phonon is included, while inconsistency between the experimental and theoretical spectra (see the dashed lines in Figure 4) is clear when this phonon is omitted.

3.2 | Raman spectroscopy

The Raman spectra of the ZnO, ZnS, and zno@zns core-shell nanostructure, measured in the spectral range of 100–600 cm^{-1} at room temperature, are presented in Figure 4. Experimental Raman scattering spectra are analyzed by the deconvolution of the Lorentzian curve.[39] The thick red line presents a resulting spectral curve. Positions of Lorentzians are given in Table 2.

The Raman spectrum of the ZnO nanoparticle is presented in Figure 4a. Intense modes at 203, 330, 379, 411, 436, 484, 540, and 578 cm^{-1} were detected. The obtained results are in good agreement with the values given in the literature,[40] as it should be for the commercially supplied materials.

When ZnS is concerned the circumstances are more complex. In our previous research[41] the ZnS nanoparticles obtained by the mechanochemical synthesis dissolved in polymethyl methacrylate (PMMA) were studied. The experimental spectrum of the ZnS nanoparticle is characterized by several broader structures, broad multimodal features in 130–200 cm^{-1} region, along with the broad structures centered at 263, 346, and 425 cm^{-1}. Like in the far-infrared spectra analysis, the phonon influence at 310 cm^{-1} was observed. Congruence of the fitted spectrum with the experimental one is better when it is performed with this phonon.

Figure 4c shows the Raman spectra of the zno@zns core-shell nanostructure. Beside the phonons which originate from the initial constituents, there are two new structures evident at 246 and 472 cm^{-1}. In addition, the structure at approximately 310 cm^{-1} is shifted to the lower wavenumbers, while phonon observed at 346 cm^{-1} originating from ZnS is shifted at 349 cm^{-1}.
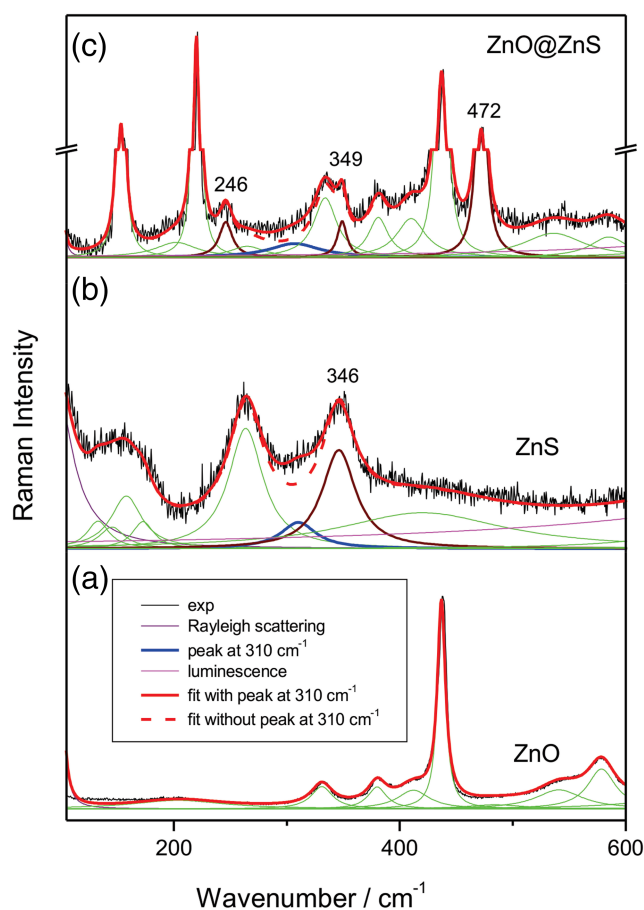
FIGURE 4 (a–c) Raman spectra for all investigated samples. The measured spectra are represented by dark line; theoretical spectra are convolution of Lorentzian curves [Colour figure can be viewed at wileyonlinelibrary.com]

4 | DISCUSSION

In the examined samples the ZnO particles are observed as big cylinders, few hundreds of nm in size. But even for the nanoparticles of few nanometers, as a consequence of the rather flat ZnO dispersion in the Brillouin zone, the effect of the optical phonons confinement is negligible, and the experimental spectra are almost the same as in the case of the bulk samples. This can also be applied to the ω_{LO} phonon of ZnS at about 350 cm^{-1}. Its shift toward the lower wavenumbers is expected and consistent with the corresponding nano dimension.[34]

Surface modes are difficult to be observed experimentally. But we roughly analyzed investigated nanoparticles (particle material, geometry, and dielectric permittivity if surrounding material), and we find that some feature in experimental spectra can be fairly good identified as surface modes. We used typical values of ZnO and ZnS dielectric parameters that are in our earlier papers: ZnO ($\varepsilon_0 = 10.24$, $\varepsilon_{besk} = 4.47$); ZnS($\varepsilon_0 = 8.1$; $\varepsilon_{besk} = 5$).

In principle, if nano-objects are present, then the surface of the whole particle is in contact with the matrix. Surface optical phonons (SOP) are characteristic when these nano-objects embedded in the matrix are concerned, and their activity becomes significant since they appear in the experimental spectra. Surface phonons are the most prominent in the spectra of the objects a few nanometers in size. The ZnO nanoparticles in the present study are cylindrical with axial symmetry. To find the wavenumbers of surface phonons the classic electrostatic equation for the appropriate geometry must be solved taking into account the interface conditions, that is, the object geometry must be treated properly.[42,43] Results of the study showed that for the cylinder-like nano-objects two types of surface phonons are characteristic: side surface optical phonons (SSO) and top surface optical phonons (TSO). SSO modes are related to the cylindrical interface (like in the cylindrical wire), and TSO modes are related to the planar interface (base of the cylinder).[42–44] There are two types of TSO mode: anti-symmetric and symmetric. Besides the geometry of the objects, surface optical frequencies are sensitive to the surface environment, that is, dielectric permittivity of the outer medium. All surface mode wavenumbers are in region $\omega_{TO} < \omega_{SOP} < \omega_{LO}$, that is, $\omega_{IITO} < \omega_{SOP} < \omega_{mixedLO} \approx 572$ cm^{-1}. In real samples spectra, surface optical wavenumbers depend on the surface quality, that is, surface roughness and arrangement and density of the nano-objects, resulting in the effective surrounding medium permittivity.

In the experimental ZnO spectra a wide feature of very low intensity is centered at ∼484 cm^{-1}. This mode can be assigned as the surface optical mode,[42,43] or even more precise as TSO.[44] In the experimental spectra, a wide feature of middle low intensity centered at about 540 cm^{-1} can also be observed. This mode can be assigned as the surface optical mode.[45]

Surface mode wavenumbers for the ZnS particles are the solution of the same equation [43] but in the spherical case. If the non-polar matrix surrounds spherical QD (case of radial, i.e., central symmetry), there is one surface mode for each quantum number l. The wavenumber of these modes does not depend on the sphere radius. In the case of ZnS QD without matrix, that is, in a vacuum ($\varepsilon_{matrix} = 1$), wavenumbers of $l = 1$ and $l = 2$ surface phonons are ∼330 and ∼334 cm^{-1}, respectively. When the matrix is concerned, it must be noted that when the dielectric permittivity is increasing to the value higher than 1, then the surface modes wavenumbers are decreasing. The calculated surface mode wavenumber ($l = 1$, $\varepsilon_{matrix} = 2$) is 310 cm^{-1}. Mode in the spectral region from 300 to 330 cm^{-1} can be assigned as the ZnS nanoparticle surface mode.[34]

In the case of ZnO@ZnS, the surface optical ZnO mode at 484 cm^{-1} (TSO) is completely screened by the impurity mode. Surface optical ZnO mode at 540 cm^{-1} is at the same position and with the almost unchanged intensity as in the ZnO nanoparticles spectra. The surface optical ZnS mode of low intensity is at position 305 cm^{-1}. It is not clear if the ZnS shell is complete and uniform over the entire ZnO cylinder, but this decrease of the surface optical mode wavenumber is a sign that ZnS is effectively in $\varepsilon_{matrix} < 2$.

Surface optical modes are treated rudimentary, and this is not the main contribution in this paper. It is a possible explanation for these low-intensity features that appear in the experimental spectra. Position of these modes gives fairly good identification.

Raman active modes registered at 246 and 472 cm^{-1} for ZnO@ZnS core-shell nanostructure (Figure 3) were not observed in starting components. It can be assumed that in this case impurity modes are in question. Considering previous observation, it seems that in this case, during the formation of the ZnO@ZnS core-shell nanostructure the phenomenon indicated in Figure 3 occurred. To be precise, in the thin layer between ZnS and ZnO migration of oxygen and sulfur took place. This indicates that oxygen originated from ZnO migrated into the ZnS lattice where it substituted sulfur, while sulfur, in the same way, migrated into the ZnO lattice. New vibrational modes, separated from the host lattice modes, can appear when the supplementary atoms are integrated into the host lattice. When the amount of the impurity atoms is minor in comparison to the amount of the host lattice atoms, the generated mode is "localized." Namely, its eigenvector doesn't have a sinusoidal or wavelike dependence on space, but is strongly peaked at the impurity atom, and wanes rapidly on one or two lattice sites away.[46]

More precisely, when the lighter element (sulfur in this case) in the binary mixture ZnS ($m_S < m_{Zn}$) is replaced by the even lighter impurity (oxygen, $m_O < m_S$), a local mode is formed above the top of the optical band of ZnS. On the other hand, when the heavier impurity (sulfur) replaces the lighter element (oxygen) within the binary mixture (ZnO) a gap-mode is formed below the bottom of the optical band of the binary mixture.

Calculation of the local-mode and gap-mode wavenumbers [47] involves a comprehension of the eigenfrequencies and eigenvectors of the host-crystal vibrational modes, as well as changes in the mass and force constant caused by the impurity atom. The mass-defect parameter $\varepsilon_j = 1 - M/M_j$ plays an important role, where M is the mass of the impurity atom and M_j is the mass of the host/crystal atom. For the limited number of the polar diatomic crystals, the three-dimensional

mass-defect calculation was performed. Using the full lattice dynamics, the additional calculations were made for particular types of impurities in some host crystals.[48–50]

Lucovsky et al.[51] established a simple model for the calculation of local modes in three-dimensional crystals. In the present case, when sulfur in ZnS is substituted with oxygen the obtained position of the local mode is 471 cm^{-1}, which is in excellent agreement with the experimentally obtained result.

In the opposite case, when the gap mode is formed as a consequence of the replacement of oxygen with sulfur in ZnO, the situation is more complex and the mass-defect parameter is $\varepsilon_j = -1$. Consequently, for this parameter value, used models show singularity and that makes them inappropriate. Because of that, the simplest way to calculate gap mode position using only isotope effect was chosen[48]; that is, only mass variation is taken into account, while the gap mode is obtained by the separation from the TO phonons of the starting crystal. Applying this method enabled the obtainment of the position of the sulfur gap-mode in ZnO at approximately 268 cm^{-1}. That is in a good agreement (difference is 9%) with the experimentally obtained position at 246 cm^{-1}.

Few crystallographic planes of crystal material must be present in the crystallite to register particular crystallographic structure of crystallite by XRD. This is not the case in the ZnO-ZnS interface region. We did not observe any peak in the XRD that originates from ZnO-ZnS mixing region. This region seems to be very narrow. But characteristics of this interface region are clearly seen from very intensive new Raman modes of ZnO-ZnS, that is, appearance of local and gap modes. Raman spectroscopy is known as sensitive to the close surrounding.

The registered phonon properties are directly related to the existence of the active layer isolated impurities in the binary system, that is, sulfur in ZnO and oxygen in ZnS. Matching of the experimentally and theoretically obtained values indicates the complete incorporation of the impurities into the binary system with all the properties that this phenomenon brings. Obtained results will be a starting point for the continuation of the research in this field toward the application of these materials as thermoelectrics.

5 | CONCLUSION

The ZnO@ZnS core-shell nanostructure with an active layer is obtained by conversion of zinc oxide powders with H_2S. SEM images and XRD patterns shown the existence of a cylindrical nanostructure confirming at the

same time that core-shell structure is usually characterized by the same morphology as a core, in this case ZnO. Using Raman and Far-infrared spectroscopy the phonons characteristics of the starting components were registered. TSO in ZnO, characteristic for the cylindrical nano-objects, the surface optical phonon (SOP) mode of ZnS as well as SOP modes in ZnO@ZnS core-shell nanostructure are registered. Local-mode of oxygen in ZnS and gap-mode of sulfur in ZnO are also registered. These results are due to the existence of an active layer in the space between the ZnO core and the ZnS shell. These findings are very important for the potential application of these materials as thermoelectrics.

ORCID

Branka Hadzic https://orcid.org/0000-0001-5459-7461
Maja Romcevic https://orcid.org/0000-0002-5064-175X

REFERENCES

[1] S. S. Kumar, P. Ventakeswarlu, V. R. Rao, *Int. Nano Lett.* **2007**, *61*, 2054.

[2] A. Kushwaha, M. Aslam, *Electrochim. Acta* **2014**, *130*, 222.

[3] K. J. Klabude, *Nanoscale Materials in Chemistry*, Wiley Intercience, New York **2001**.

[4] N. Romcevic, R. Kostic, B. Hadzic, M. Romcevic, I. Kuryliszyn-Kudelska, W. D. Dobrowolski, U. Narkiewicz, D. Sibera, J. Alloys, *Compd.* **2010**, *507*, 386.

[5] J. M. Azpiroz, E. Mosconi, F. De Angelis, J. Phys. Chem. C **2011**, *115* (*51*), 25219.

[6] P. V. Raleaooa, A. Roodt, G. G. Mhlongo, D. E. Motaung, R. E. Kroon, O. M. Ntwaeaborw, *Physica B Condens. Matter* **2017**, *507*, 13.

[7] C. W. Raubach, Y. V. De Santana, M. M. Ferrer, P. G. Buzolin, J. R. Sambrano, E. Longo, *Dalton Trans.* **2013**, *42*, 11111.

[8] M. Sookhakian, Y. M. Amin, W. J. Basirun, M. Tajabadi, N. Kamarulzaman, *J. Lumin.* **2014**, *145*, 244.

[9] G. Homm, M. Piechotka, A. Kronenberger, A. Laufet, F. Gather, D. Hartung, C. Heiliger, B. Mayer, P. Klar, S. Steinmller, J. Janek, *J. Electron. Mater.* **2010**, *39*, 1504.

[10] G. Homm, J. Teubert, T. Henning, P. J. Klar, B. Szyszka, *Phys. Status Solidi C* **2010**, *7*(6), 1602.

[11] M. Bachmann, M. Czerner, S. Edalati-Boostan, C. Heiliger, *Eur. Phys. J. B* **2012**, *85*, 146.

[12] J. Huso, J. R. Ritter, L. Bergman, M. D. McCluskey, *Phys. Status Solidi B* **2019**, *256*, 1800607.

[13] M. Bachmann, M. Czerner, C. Heeliger, *Phys. Status Solidi A* **2013**, *210*(1), 125.

[14] K. L. Pisane, S. K. Singh, M. S. Seehra, *J. Appl. Phys.* **2015**, *117* (*17*), 17D708.

[15] A. V. Nomoev, S. P. Bardakhanov, M. Schreiber, D. G. Bazarova, N. A. Romanov, B. B. Baldanov, B. R. Radnaev, V. V. Syzrantsev, *Beilstein J. Nanotechnol.* **2015**, *6*, 874.

[16] A. M. El-Toni, M. A. Habila, J. P. Labis, Z. A. Althman, M. Alhoshan, A. A. Elzatahry, F. Zhangg, *Nanoscale* **2016**, *8*, 2510.

[17] S. Hou, Y. Chi, Z. Zhao, *IOP Conf. Ser. Mater. Sci. Eng.* **2017**, *182*, 012026.

[18] Y. F. Zhu, D. Fan, W. Shen, *J. Phys. Chem. C* **2008**, *112*, 10402.

[19] M. Sundararajan, P. Sakthivel, A. C. Fernandez, J. Alloys, *Compd.* **2018**, *768*, 553.

[20] E. M. Flores, C. W. Raubach, R. Gouvea, E. Longo, S. Cava, M. L. Moreira, *Mater. Chem. Phys.* **2016**, *173*, 347.

[21] K. T. Lee, B. H. Choi, J. U. Woo, J. S. Kang, J. H. Paik, B. U. Chu, S. Nahm, *J. Europ. Ceramic Soc.* **2018**, *38*, 4237.

[22] B. S. Rema Devi, R. Raveendrana, V. Vaidyan, *Pramana – J. Phys.* **2007**, *68*(4), 679.

[23] E. Zheng, Y. Wang, J. Song, X. F. Wang, W. Tian, G. Chen, T. Miyasaka, *J. Energy Chem.* **2018**, *27*(5), 1461.

[24] P. V. Raleaooa, A. Roodt, G. G. Mhlongo, D. E. Motaung, R. E. Kroon, O. M. Ntwaeaborwa, *Phys. B* **2017**, *507*, 13.

[25] Powder Diffraction File, PDF-2 Database, announcement of new data base release **2012**, International Centre for Diffraction Data (ICDD).

[26] C. Suryanarayana, M. Grant Norton, *X-ray Diffraction: A Practical Approach*, Springer, New York **1998** Version 2012.

[27] T. Ghrib, M. A. Al-Messiere, A. L. Al-Otaibi, *J. Nanomater.* **2014**, *2014*, 989632.

[28] J. Han, W. Liu, T. Zhang, K. Xue, W. Li, F. Jiao, W. Qin, *Sci. Rep.* **2017**, *7*, 42536.

[29] P. Banerjee, P. K. Jain, *RSC Adv.* **2018**, *8*, 34476.

[30] A. K. Kole, P. Kumbhakar, *Results Phys.* **2012**, *2*, 150.

[31] T. Ungar, *J. Mater. Sci.* **2007**, *42*, 1584.

[32] B. Hadzic, N. Romcevic, M. Romcevic, I. Kuryliszyn-Kudelska, W. Dobrowolski, J. Trajic, D. Timotijevic, U. Narkiewicz, D. Sibera, J. Alloys, *Compd.* **2012**, *540*, 49.

[33] P. Bruesch, *Phonons: Theory and experiments II* **1986**, 2. United States: Springer-Verlag New York Inc.

[34] J. Trajic, R. Kostic, N. Romcevic, M. Romcevic, M. Mitric, V. Lazovic, P. Balaz, D. Stojanovic, J. Alloys, *Compd.* **2015**, *637*, 401.

[35] G. Abstreiter, M. Cardona, A. Pinczuk, in *Light Scattering in Solids, IV*, Ed. By M. Cardona and G. Guntherodt (Springer-Verlag, Berlin, **1984**).

[36] E. Burstein, A. Pinczuk, R. F. Wallis, in *The Phys. of Semimetals and Narrow-Gap Semicon*, (Eds: D. L. Carter, R. T. Bate), Pergamon, New York **1971**.

[37] A. Sihvola, *IEE Electromagnetic Waves Series* **1999**, *47*.

[38] J. C. Maxwell Garnett, *Phil. Trans. R. Soc. A.* **1904**, *203*, 385.

[39] B. H. Henry, J. R. During (Eds), *Raman spectroscopy: Sixty Years On*, Vol. 10, Elsevier, Amsterdam **1990**.

[40] B. Hadzic, N. Romcevic, M. Romcevic, I. Kuryliszyn-Kudelska, W. Dobrowolski, R. Wróbel, U. Narkiewicz, D. Sibera, J. Alloys, *Compd.* **2014**, *585*, 214.

[41] M. Curcic, B. Hadzic, M. Gilic, V. Radojevic, A. Bjelajac, I. Radovic, D. Timotijevic, M. Romcevic, J. Trajic, N. Romcevic, *Physica E Low Dimens. Syst. Nanostruct.* **2020**, *115*, 113708.

[42] P. M. Chassaing, F. Demangeot, V. Paillard, A. Zwick, N. Combe, *Appl. Phys. Lett.* **2007**, *91* (*5*), 053108.

[43] P. M Chassaing, F. Demangeot, V. Paillard, A. Zwick, N. Combe, C. Pagès, M. L. Kahn, A. Maisonnat, B. Chaudret, *J Phys Conf Ser.* **2007**, *92*, 012165.

[44] P. M. Chassaing, F. Demangeot, V. Paillard, A. Zwick, N. Combe, C. Pages, M. L. Kahn, A. Maisonnat, B. Chaudret, *Phys. Rev. B* **2008**, *77*, 153306.

[45] A. Pescaglini, E. Secco, A. Martin, D. Cammi, C. Ronning, A. Cantarero, N. Garrob, D. Iacopino, *J. Mater. Chem. C* **2016**, *4*, 1651.

[46] A. S. Baker, A. J. Sievers, *Rev. Mod. Phys.* **1975**, *47*, S1.

[47] P. G. Dawber, R. J. Elliott, *Proc. Roy. Soc. (London)* **1963**, *A273*, 222.

[48] J. Mitric, U. Ralevic, M. Mitric, J. Cirkovic, G. Krizan, M. Romcevic, M. Gilic, N. Romcevic, *J. Raman Spectrosc.* **2019**, *50* (6), 802.

[49] R. Kostic, M. Petrovic-Damjanovic, N. Romcevic, M. Romcevic, D. Stojanovic, M. Comor, J. Alloys, *Compd.* **2012**, *521*, 134.

[50] I. F. Chang, S. S. Mitra, *Phys. Rev.* **1968**, *172*(3), 924.

[51] G. Lucovsky, M. H. Brodsky, E. Burstein, *Phys. Rev. B* **1970**, *2*, 3295.

SUPPORTING INFORMATION

Additional supporting information may be found online in the Supporting Information section at the end of this article.